Oxidation Control to Augment Interfacial Charge Transport in Te-P3HT Hybrid Materials for High Thermoelectric Performance

Syed Zulfiqar Hussain Shah[1,2*], Ding Zhenyu[5], Zainul Aabdin[1], Weng Weei Tjiu[1], Jose Recatala-Gomez[3], Haiwen Dai[3], Yang Xiaoping[5], Repaka Durga Venkata Maheswar[1], Wu Gang[4#], Kedar Hippalgaonkar[1, 3#], Pawan Kumar[1#], Iris Nandhakumar[2#]

1. Institute of Materials Research and Engineering, Agency for Science Technology and Research (A*STAR), Singapore 138634, Republic of Singapore.
2. Department of Chemistry, University of Southampton, Southampton SO17 1BJ, United Kingdom.
3. School of Materials Science and Engineering, Nanyang Technological University, 50 Nanyang Avenue, Block N4.1, 639798, Singapore.
4. Institute of High-Performance Computing, Agency for Science Technology and Research (A*STAR), Singapore 138632, Republic of Singapore.
5. High Magnetic Field Laboratory, Chinese Academy of Sciences, University of Science and Technology of China, No.96, JinZhai Road Baohe District, Hefei, Anhui, 230026, P.R. China

* First Author, Corresponding Authors[#]

The combination of inorganic nanostructured materials within organic conducting polymers have attracted tremendous interest for designing new organic-inorganic hybrid thermoelectric (TE) materials for harvesting waste heat energy. Due to their mechanical flexibility and simple fabrication process, inorganic-organic hybrid TE materials are considered to be promising candidates for flexible energy harvesting devices. In this work, we report enhanced TE properties of Tellurium (Te) nanowires (NWs)- poly (3-hexylthiophene-2, 5-diyl) (P3HT) hybrid materials by improving the charge transport at interfacial layer mediated via controlled oxidation and optimizing the doping efficiency of the $FeCl_3$ dopant. A power factor of ~ 9.8 $\mu W/mK^2$ was obtained at room temperature for oxidised P3HT-TeNWs hybrid materials which increases to ~ 64.8 $\mu W/mK^2$ upon control of TeNWs oxidation. This value is seven-fold higher compared to P3HT-TeNWs based hybrid materials reported in the literature. MD simulation reveals that oxidation free TeNWs demonstrate better templating for P3HT polymer compared to oxidised TeNWs. The Kang-Snyder model was used to study the charge transport in these hybrid materials. A large σ_{E0} value was obtained which is related to better templating of P3HT on oxygen free TeNWs. Our work provides evidence that oxidation control of TeNWs is critical for better

interface-driven charge transport which enhances the thermoelectric properties of TeNWs-P3HT hybrid materials. Our work provides new avenue to improve thermoelectric properties of new class of hybrid thermoelectric materials.

Keywords: Thermoelectric materials, thin film, power factor, electrical conductivity, Seebeck coefficient, nanomaterials, P3HT polymer, hybrid material, doping, microstructural characterization.

Introduction

Thermoelectric (TE) devices have the ability to directly convert heat into electricity, without the need for moving parts.[1,2] The efficiency of a TE device is related to the dimensionless figure of merit (zT) which is defined as $zT = \frac{S^2\sigma T}{\kappa}$, where S is the Seebeck coefficient, σ is the electrical conductivity, T is the absolute temperature, κ is the thermal conductivity, and $S^2\sigma$ is the power factor (PF) of the TE material.[2] A low κ and high PF are hence required to achieve better performing TE materials. Due to the strong interdependence of transport parameters (S, σ, and κ) optimizing the TE performance is a complex task. Nanostructuring of inorganic materials is a promising strategy to control these interdependencies and significant improvements in zT of inorganic thermoelectric materials have been achieved recently.[2,3] Substantial research endeavors have been dedicated to incorporating these nanostructured inorganic materials into the matrix of conducting polymers in recent years.[4-16] For example, Wang et al.,[5] synthesized a PANI-Te composite which exhibited a Seebeck coefficient of 102 μV/K, electrical conductivity (σ) of 102 S/cm, and a power factor (PF) of 105 μW/m-K^2. Sahu reported a PF of 145 μW/mK^2 for PEDOT:PSS/TeNWs,[18] and Gordon achieved a PF of 130 μW/m-K^2 at room temperature using PEDOT:PSS/TeNWs.[19] Nevertheless, numerous polymer/inorganic composites, primarily employing conducting polymers, have been recorded to demonstrate a significant thermoelectric power factor exceeding 100 μW/mK^2.[5,12,17-20]

Conversely, polymer/inorganic composites based on P3HT have been explored to a limited extent so far. For instance, Ming He et al.,[4] incorporated Bi_2Te_3 nanowires (NWs) into P3HT, yielding a composite with a power factor of 13.6 μW/m-K^2. Liang studied the P3HT/TeNWs composite system, achieving an electrical conductivity of 21.3 S/cm, Seebeck coefficient of 67.1 μV/K, and a power factor of ~ 9.59 μW/mK^2 with optimal 30% $FeCl_3$ doping.[11] Interfacial transport,

structural/morphological effects, and modifications to the energy dependence of carrier scattering (energy filtering) to improve electronic and thermoelectric performance have been suggested to explain the charge transport in these hybrid materials.[4,11,21-23] Later Kumar et al.,[24] demonstrated that the high thermoelectric performance observed in these complex hybrid systems can be explained by physical interfacial interactions between the inorganic and organic component which enhance the Seebeck coefficient and carrier mobility in these hybrid materials. Experimentally a highly ordered morphology of conducting polymers has been demonstrated through interfacial interactions with inorganic nanostructures at interface which give rise to high electrically conductive path for charge carriers.[22,24,37,38] Besides, It has been demonstrated that these inorganic nanostructures are prone to oxidation which potentially affect the thermoelectric properties of these hybrid materials.[25]

In this work we have improved the interfacial interaction of Te-P3HT hybrid materials through controlled oxidation. Our findings highlight a substantial improvement in the power factor of the P3HT-TeNWs hybrid nanocomposites. We demonstrate that precise oxidation control during the synthesis of inorganic TeNWs and the preparation of the hybrid film is crucial for improving the templating of P3HT along the TeNWs, and ultimately improving the interfacial transport within the hybrid material. The resulting P3HT-TeNWs thermoelectric nanocomposites exhibited the highest power factor of 64.8μW/mK^2 at room temperature. This achievement represents a sevenfold increase in comparison to previously documented values in the literature [SI Fig. S11].[11] Due to the inherently low thermal conductivity of these hybrid materials [4,5,17] our optimization efforts focused on enhancing the power factor of the P3HT-TeNWs composite hybrid material (instead of zT) and the interfacial layer by controlling the oxidation level to optimize the charge transport properties in these systems.

Results and Discussion

P3HT-TeNWs nanocomposite hybrid films with varying TeNWs to P3HT ratios (10-90 wt.%) were prepared by dispersing the P3HT-TeNWs powder in chloroform followed by drop casting. Optical micrographs of the resulting films show a uniform thermoelectric thin film [SI Fig.S1]. The thickness of P3HT-TeNWs nanocomposite films was measured by surface profilometry and varied from 5±0.87μm to 12±2.82μm with lower concentrations of Te nanowires yielding thicker films. To identify the elemental species and measure the oxidation level within the fabricated thin

films, X-ray photoelectron spectroscopy (XPS) was performed, and the results are shown in Fig.1. The XPS survey spectra in Fig.1(a &b) (up to 1200 eV) revealed the presence of tellurium, carbon, and oxygen. All spectra were calibrated with respect to the carbon C 1s peak at 284.8 eV. Core-level peaks corresponding to Te 3d, C 1s, and O 1s were observed in thin films of oxidized tellurium and oxidation-controlled tellurium nanowires. The O 1s peak around 530 eV corresponds to TeO_2 which originates from an oxidised TeNWs surface [see high resolution O 1s spectra in SI Fig. S9-b].[27] Peaks centered at a binding energy of 573.07 eV and 583.3 eV are attributed to the Te $3d_{5/2}$ and Te $3d_{3/2}$ core levels respectively, indicating that tellurium is in its metallic state.[28] In Fig 1(c) there are observable peaks at 576 eV and 586 eV that indicated an oxidized surface of tellurium NWs with 45 atomic percent oxygen content within 5-10 nm depth of the film.[29] Fig 1(d) indicates that the oxygen content is reduced to 12 atomic percent at the surface of the NWs prepared by oxidation control within 5-10 nm depth of the film. The oxygen atomic percentage is determined from the survey spectra and subsequently compared with the high-resolution Te 3d spectra, showing matching values in both scenarios. In addition, we computed the ratio of Te $3d_{5/2}$-oxide to Te $3d_{5/2}$-metal, resulting in a decrease from 0.8 to 0.2 for oxidized-TeNWs and oxidation-controlled-TeNWs, respectively.

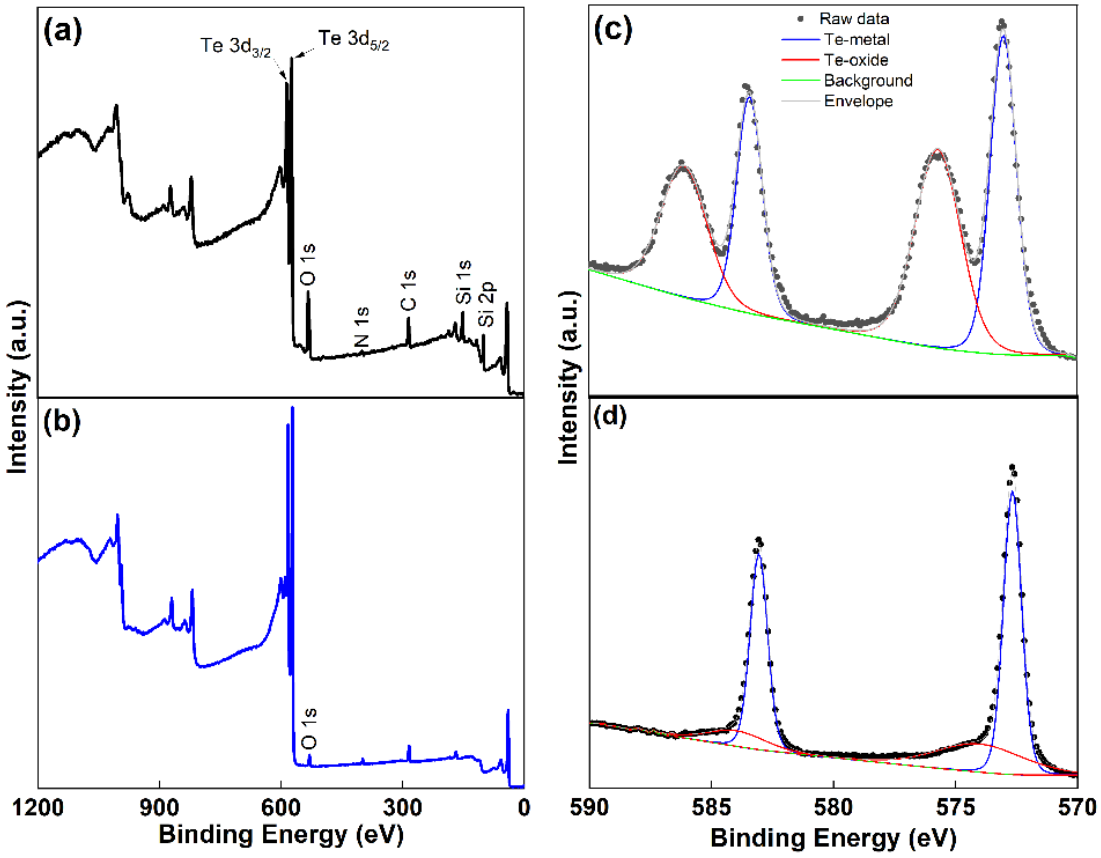

Fig. 1: **High-resolution X-ray photoelectron spectroscopy (XPS) spectra of oxidized TeNWs films and oxidation control TeNWs**: Survey scan and XPS core level spectra of Te 3d of highly oxidized TeNWs (a & c), and oxidation controlled TeNWs (b & d), respectively. Lower oxidation level was observed in oxidation controlled TeNWs compared to oxidized TeNWs.

The peak around 400.5 eV is identified as the sole nitrogen peak, possibly resulting from the use of hydrazine hydrate as a reducing agent during synthesis. Additionally, as the samples were prepared on Si substrates, the characteristic peaks at binding energies around 100.01 eV and 151.09 eV are attributed to Si 2p and Si 1s, respectively.[36]

Detailed microstructural characterizations were performed by using Scanning Electron Microscope (SEM) and Transmission Electron Microscope (TEM) to investigate the distribution of Te nanowires within the P3HT polymer matrix and the uniformity of the polymer coating on individual nanowires [SI Fig. S2-S3]. A homogenous dispersion of TeNWs within P3HT matrix is observed for all concentrations in the SEM images [SI Fig. S2, S2-b]. TEM images acquired from individual TeNWs and P3HT-TeNWs nanowires show that the microstructures of both TeNWs and P3HT-TeNWs are identical, with P3HT-TeNWs having a uniform conformal coating of the polymer (P3HT) layer on the surface of the nanowires [Fig. 2a-b and 2e-f]. The thickness of the coating is measured to be about 5 nm. High-resolution TEM (HR-TEM) images combined with selected area electron diffraction (SAED) reveal that the nanowires are single crystalline, and their c-axis is always aligned along the length of the nanowires with an interplanar spacing of ~ 0.59 nm that corresponds to the (001) reflection. Furthermore, the nanowires have a hexagonal shape, bounded by six (100) facets with measured interplanar spacing of ~ 0.39 nm along all facets, as seen in the cross-section HR-TEM images [SI Fig. S4-S5]. Low-magnification TEM images show that the TeNWs are quite uniform in diameters (~ 65±12 nm), although the nanowire length varies from a few hundred nanometers to several micrometers (~ 500-4000 nm).

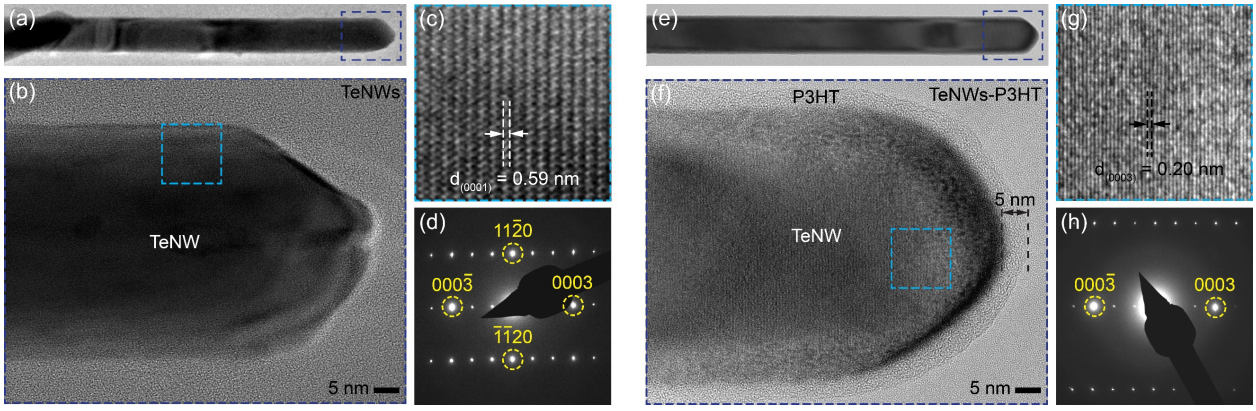

Fig. 2: High resolution TEM and selected area electron diffraction (SAED) of individual TeNW and P3HT coated TeNW. High-resolution TEM images showing the morphology of individual NWs of (a-c) TeNWs and (e-g) P3HT-TeNWs with a uniform conformal coating of the amorphous polymer (P3HT) layer on the surface of the nanowire. Selected area electron diffraction pattern of a single (d) TeNWs and (h) P3HT-TeNWs.

For optimal performance of the hybrid materials, the nanowires surface should be free from any impurities and oxide. Therefore, we performed Scanning Transmission Electron Microscope (STEM) imaging and Electron Energy Loss Spectroscopy (EELS) mapping to measure the oxygen content at the nanoscale. For both techniques, we used a probe size of about 1 nm. No oxygen traces were found in the Te-NWs [Fig. 3(a)], whereas the nanowires in Fig. 3(b) clearly show the presence of oxygen around the edges of the nanowires (green color maps) and an overall increase in the oxygen signal in the spectra [Fig. 3(c)]. This indicates surface oxidation of the Te-NWs (hereafter we will refer to them as TeO_2-NWs). A closer look at the overlay maps and line-profiles obtained for the nanowire presented in Fig. 3(d) reveals that the nanowire core is free from oxidation for both Te-NWs and TeO_2-NWs, whilst only the surface of the nanowire is oxidized for TeO_2-NWs. It is worthwhile to note that the Carbon (C) (blue maps in both cases) signal present in the EELS data does not originate from the synthesis process of the nanowires, instead, C was deposited as part of the FIB cross-section sample preparation to protect the nanowire surface from beam damage during FIB cutting. High-resolution TEM images of the oxide layer formed at the nanowire surface or at the interface of two nanowires show that the oxide layer is crystalline in nature [SI Fig. S6(c)]. Interestingly, the oxidation phenomena not only affect the nanowire surface, but introduces a lot of defects inside the Te core as seen in the TEM/STEM images presented in SI [Fig. S6-S8]. This is most likely due to the structural changes that occur at the Te nanowire surface due to oxide formation. It is worthwhile to note that Te exhibits a hexagonal crystal structure (with lattice constant a = b = 4.19 Å, c = 5.98 Å), whereas TeO_2 exhibits a tetragonal crystal structure (with lattice constant a = b = 5.41 Å, c = 13.20 Å).[27,30] It is also revealed in X-rays diffraction patterns in SI Fig. S9.

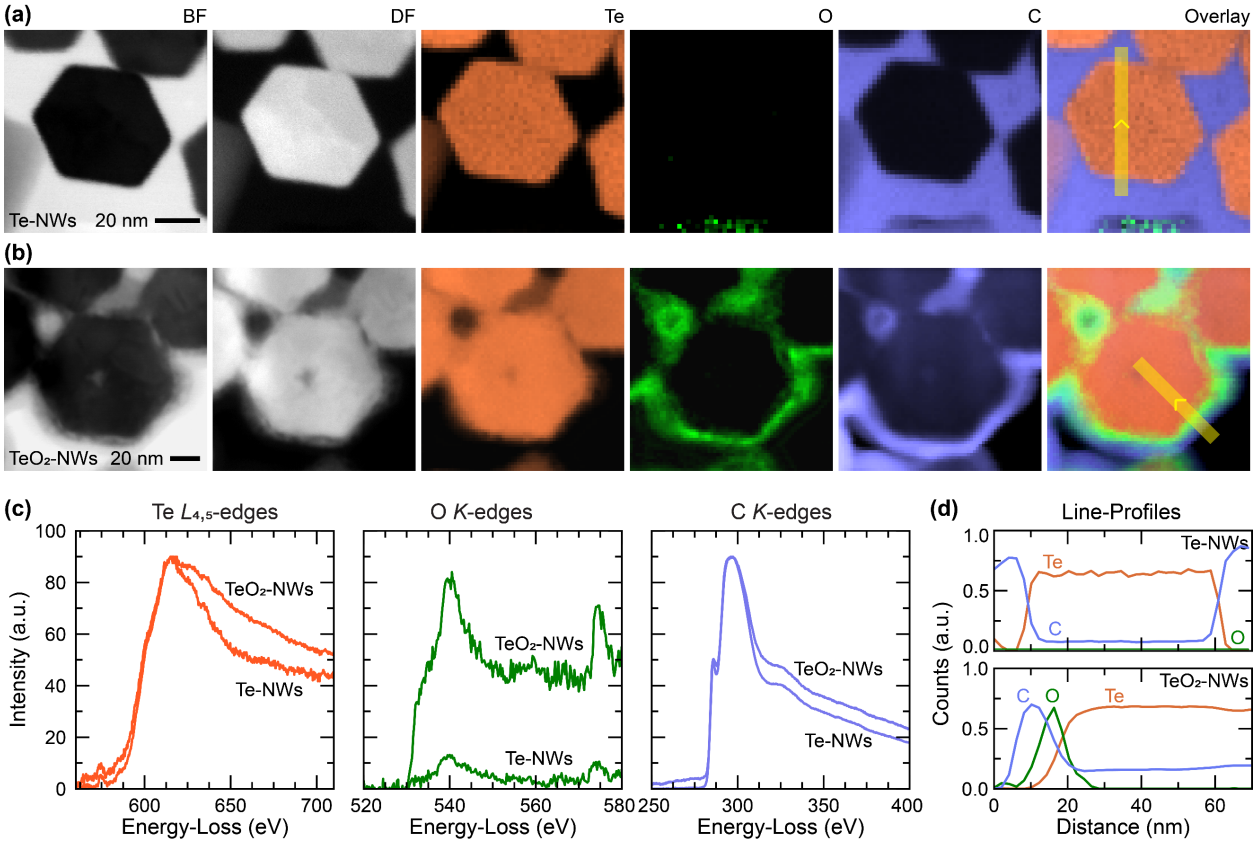

Fig. 3: Scanning Transmission Electron Microscope (STEM) imaging and Electron Energy Loss Spectroscopy (EELS) mapping to measure the oxygen content in oxidized TeNWs and oxidation controlled TeNWs.
Bright-field (BF), dark-field (DF) STEM images, corresponding elemental (Te, O, C) EELS maps, and overlay (Te + O + C) maps of the (a) Te-NWs and (b) TeO_2-NWs in cross-section. (c) Te $L_{4,5}$-edges, O *K*-edges, and C *K*-edges for the two cases extracted from the spectral image. (d) Averaged and normalized line-profile across the nanowire marked with the yellow strips in (a & b). No oxidation was observed on the surface of controlled oxidation TeNWs while a thin layer of oxidation was seen on oxidized TeNWs.

The hybrid films comprising different weight percent (wt%) ratios of TeNWs and P3HT were immersed in 0.03M $FeCl_3$ solution for doping before measuring their TE transport properties. The Seebeck coefficient, and electrical conductivity of P3HT-TeNWs nanocomposite hybrid films were measured by standard methods as detailed in the experimental section. Fig. 4a presents the thermoelectric transport properties of P3HT-TeNWs hybrid and P3HT-TeO_2NWs hybrid films as a function of varying concentrations (by weight) of NWs. For the P3HT-TeNWs hybrid system, it can be observed that with increasing concentration of TeNWs, the Seebeck coefficient increases monotonically (cf, black arrows) in Fig.4a. The Seebeck coefficient changed from 17.8±0.81 μV/K to 528.8±4.23 μV/K by increasing the TeNWs concentration from 0 to 100%. The electrical conductivity also increases initially with increasing TeNWs content (cf. black circles) in Fig. 4(a). It increases from ~11 S/cm to ~34 S/cm when the TeNWs content is increased from 0 to 60 wt%, and then remains constant at ~20 S/cm (70-90% TeNWs) before declining to ~0.02 S/cm (100%

TeNWs). The similar trend has been observed in TeNW-PEDOT: PSS system.[22] The trends for the P3HT-TeO_2NWs hybrid system are similar where conductivity (red circles) initially increases with NWs content and reaches ~35 S/cm for 30 % NWs content. Then, it drops as the NW content increases further up to ~ 5 S/cm for 90 % NWs content. On the other hand, the Seebeck coefficient (red arrows) increase monotonically with increasing NW content. Figure 4(b) shows the power factor as a function of NW content for P3HT-TeNWs (black stars) and P3HT-TeO_2NWs (red stars) hybrid systems. While the power factor for P3HT-TeNWs increases from 0.34 μW/mK^2 (0% TeNWs) to 49.8 μW/mK^2 (90% TeNWs) for doped P3HT-TeNWs hybrid system, it increases from 0.34 μW/mK^2 (0% TeNWs) to ~ 15 μW/mK^2 (80% TeO_2NWs) for P3HT-TeO_2NWs hybrid films.

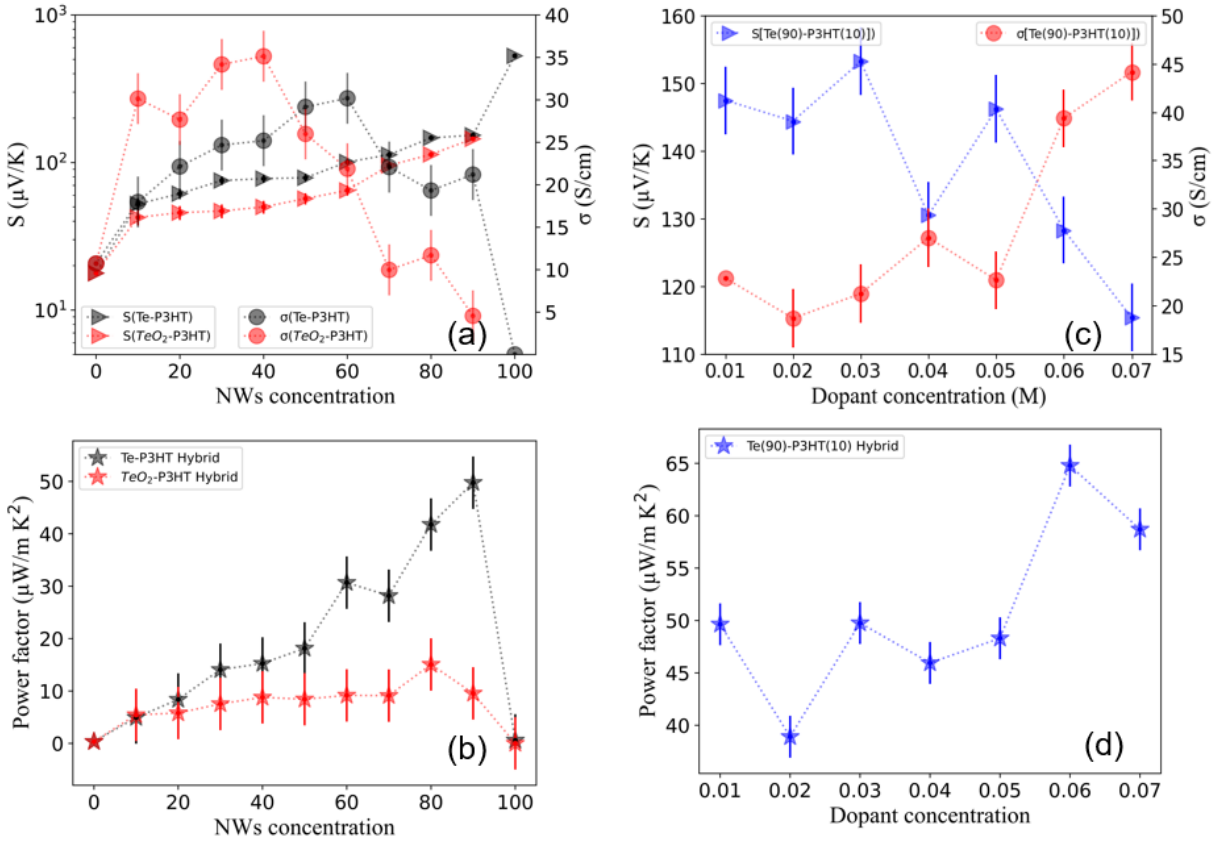

Fig. 4: Thermoelectric properties of P3HT based inorganic (TeNWs & TeO_2NWs) hybrid systems as a function of TeNWs content and dopant concentration. (a) Electrical conductivity and Seebeck coefficient & (b) power factor of 0.03M $FeCl_3$ doped hybrid films as a function of weight ratio of NWs in the P3HT matrix range from 0 wt% to 100 wt%. (c) Electrical conductivity and Seebeck coefficient & (d) power factor as a function of molar concentration of $FeCl_3$ dopant for P3HT-TeNWs hybrid films with 90 wt% TeNWs concentration. The vertical error bars represent the standard deviation of multiple measurements with respect to average values for each sample.

The P3HT-TeNWs hybrid sample with the highest power factor (90 wt% TeNWs) was selected for further optimization of the TE properties by tuning the doping level. Seven hybrid films were

fabricated and immersed in varying molar concentrations (0.01 M to 0.07 M) of $FeCl_3$-acetonitrile solutions to analyse TE trends in P3HT-TeNWs hybrid films and are shown in Fig.4 (c) and (d). Doping of the hybrid films with different concentrations of $FeCl_3$ introduces more charge carriers at the P3HT-TeNWs interface which contributes to enhancing the electrical conductivity of the hybrid films. On the other hand, increasing the carrier concentration leads to a decrease in the Seebeck coefficient [see SI Fig. S10].[31,32] Fig.4 (c) shows that the Seebeck coefficient decreases from 147.48 μV/K to 115.3 μV/K when the molar concentration of $FeCl_3$ increases from 0.01 M to 0.07 M. The electrical conductivity changed from 22.8 S/cm to 44.2 S/cm by changing the dopant concentration from 0.01 M to 0.07 M. The power factor of the hybrid films also increases with increasing $FeCl_3$ concentration reaching a maximum value of 64.8 μW/mK^2 at 0.06 M as shown in Fig.4 (d). This suggests that incorporation of nanowires within a conducting polymer matrix could effectively enhance the power factor of nanocomposite hybrid materials at the optimum doping level using a suitable dopant concentration.

Next, we studied the charge transport in the P3HT-TeNWs hybrid system (90wt% TeNWs-10% P3HT) using the Boltzmann Transport framework as developed for conducting polymers by Kang and Snyder (Kang-Snyder Model).[26] According to the Kang-Snyder model, the energy-dependent conductivity $\sigma_E(E,T)$ can be expressed as:

$$\sigma_E(E,T) = \sigma_{E_0}(T)\left(\frac{E-E_t}{k_B T}\right)^s \quad (1)$$

Where, E_t is the transport edge (energy) below which conductivity has no contribution even at finite temperature, 's' is the energy-dependent scattering parameter and 'σ_{E0}' is the energy-independent transport parameter to model the TE transport of conducting polymers over a large range of conductivities. k_B is the Boltzmann constant. The total conductivity is given by:

$$\sigma = \int_0^\infty \sigma_E(E,T)\left(-\frac{\partial f}{\partial E}\right) dE \quad (2)$$

By inserting equation (1) into equation (2), and integrating by parts, the total conductivity can be expressed as:

$$\sigma = \sigma_{E_0}(T) \times sF_{s-1}(\eta) \quad (3)$$

Where $\eta = \frac{E_F-E_t}{k_B T}$ is the reduced chemical potential and F is the Fermi integral. The corresponding Seebeck coefficient (S) can be expressed as:

$$S = \frac{k_B}{e}\left[\frac{(s+1)F_s(\eta)}{sF_{s-1}(\eta)} - \eta\right] \quad (4)$$

The reduced chemical potential (η) is determined by using the experimental values of the Seebeck coefficient for a specific value of the energy dependent parameter *s*. Figure 5(a) shows the Seebeck coefficient as a function of conductivity for the P3HT-TeNWs hybrid sample (90%TeNWs-10% P3HT). The data was collected by performing de-doping experiments. During the de-doping process, the sample was heat treated at 50°C to slowly remove the dopant which resulted in a drop of the electrical conductivity. As expected, the Seebeck increases with decreasing conductivity. Power factor was observed to drop gradually with decreasing electrical conductivity.

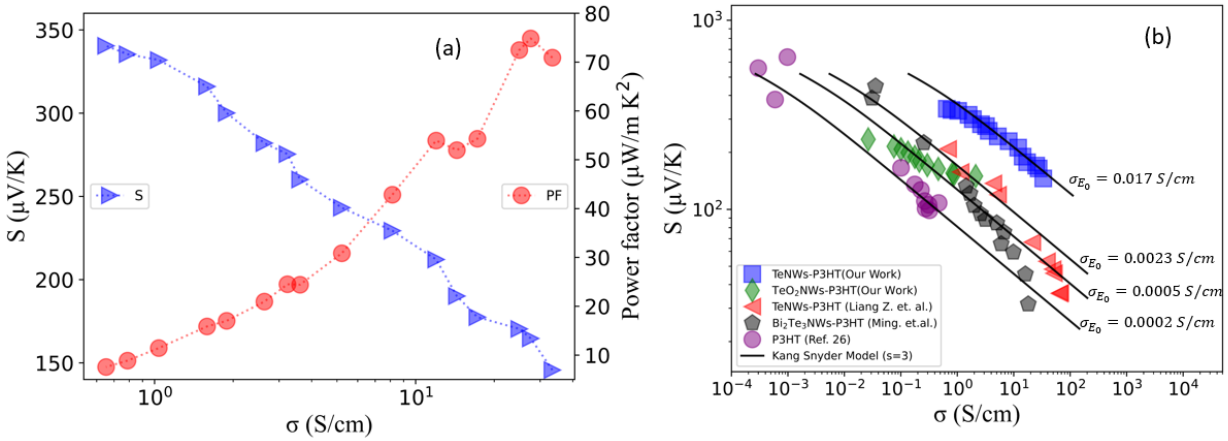

Fig. 5: **The Kang-Snyder charge transport (CT) model applied to P3HT based nanocomposite hybrid systems**. (a) The experimental Seebeck (S) vs electrical conductivity (σ) data of 0.06M $FeCl_3$ doped P3HT-TeNWs hybrid system (b) The electrical conductivity vs Seebeck coefficient data of P3HT-TeNWs (blue square) from this work, TeO_2NWs-P3HT (green diamond) from this work, P3HT-TeNWs (red triangles, Liang et. al.,), Bi_2Te_3-P3HT (grey pentagons, Ming et. al.,), and pure P3HT (purple circles, Ref. 26). Our experimental data lies on the energy dependent scattering parameter s = 3 curve with energy independent transport parameter σ_{E0} = 0.017 S/cm.

Fig. 5(b) shows the Seebeck coefficient as a function of the electrical conductivity of P3HT-TeNWs [blue squares, this work], P3HT-TeO_2NWs [green diamond, this work], P3HT-TeNWs [red triangles, Liang et al.][11], pure P3HT [purple circles, Kang and Snyder][26], Bi_2Te_3-P3HT [grey pentagons, Ming H. et al.].[4] The Kang-Snyder model was applied to these systems. As can be seen in Fig. 5(b) the experimental data for all the different P3HT based hybrid materials exhibit an energy dependent scattering parameter of s= 3. For our P3HT-TeNWs hybrid system σ_{E0} was found to be 0.017 S/cm which is one order higher compared to P3HT-TeNWs hybrid system reported in the literature.

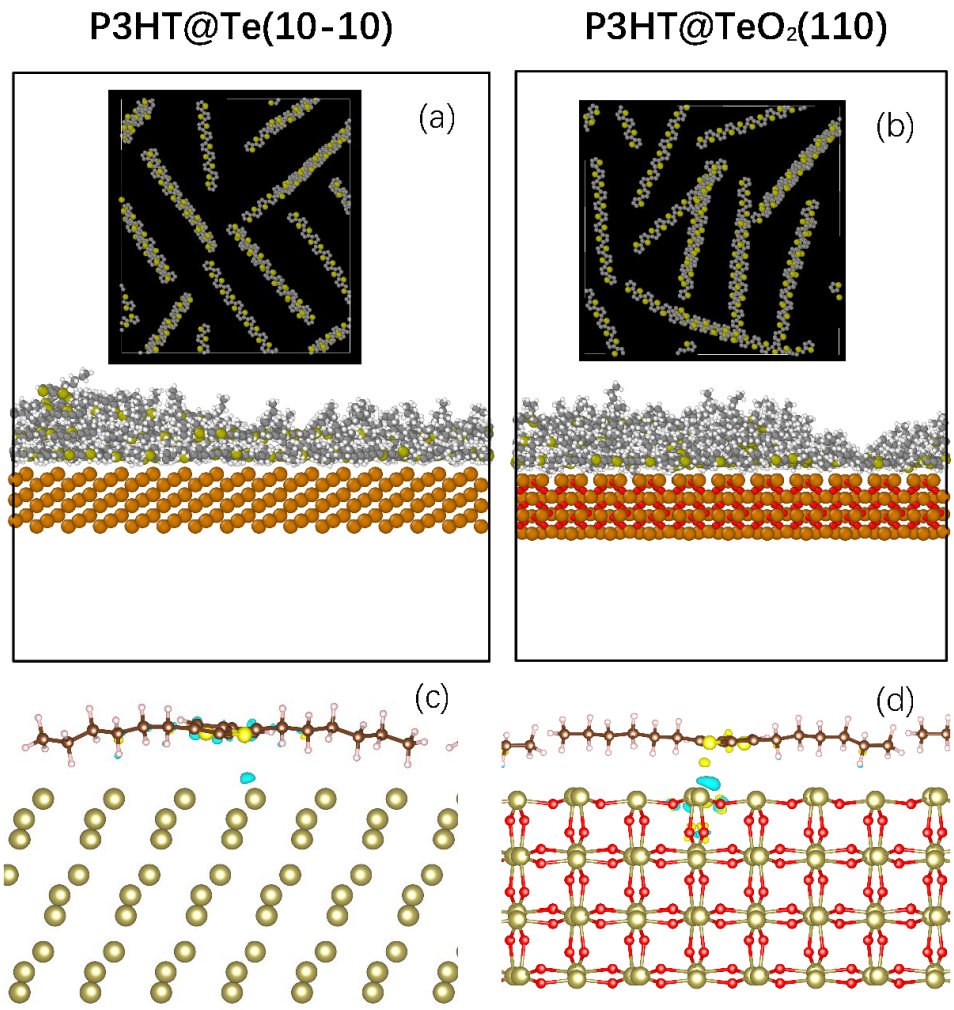

Fig. 6: MD simulation of P3HT polymer morphology and alignment at the organic-inorganic interface on Te and TeO_2 surface. Here, the final polymer structures are depicted after simulated annealing of five chains of P3HT on (a) Te (hexagonal) and (b) TeO_2 (tetragonal) surfaces. There is a high concentration of S atoms of P3HT observed at 3–5 Å from the nanowire surfaces, suggestive of highly ordered and aligned P3HT chains at the organic-inorganic interface. Although alignment occurs, self-assembly of chains is reduced on TeO_2 compared to the Te surface. (c) DFT calculations reveal electronic effects at the organic-inorganic interface. Electrons transfer from Te surface to P3HT chains monitored by increase of electron density (yellow) on P3HT and at the interface and decrease of electron density (cyan) at the Te phase. (d) Electron transfer from TeO_2 to P3HT. The iso-values in (c) and (d) are 10^{-3} and 2.5×10^{-3} $Å^{-3}$, respectively. Obviously, the amount of charge transfer is more significant in the case of TeO_2 substrate.

In order to explain the higher value of σ_{E0} and the conductivity trend, we performed molecular dynamics (MD) simulations to understand the ordering of P3HT polymer on both Te and TeO_2 surface. Whilst P3HT aligns preferentially on a pristine Te surface, a different preferential orientation of P3HT was observed on a TeO_2 surface (Figure. S16). Our findings reveal that the templating is more effective on the Te surface compared to a TeO_2 surface as shown in Figure 6(a) and (b). To initialize the MD simulations, we assumed TeO_2 to adopt a crystalline tetragonal structure, as observed experimentally in TEM. However, it is important to note that while the interface between Te core and TeO_2 exhibits a crystalline nature, the regions further from the

interface display an amorphous oxide [Figure S6(c)]. As a result, we anticipate that the polymer templating will be even less efficient for TeO_2 nanowire, leading to a lower value of σ_{E0}, as observed in Figure 5.

The highest value of σ_{E0} is observed for Te-P3HT hybrid material, primarily due to a better templating of P3HT on Te surface, as supported by MD simulations. Figure 6(c) and (d) demonstrate the charge transfer from the inorganic surface to the first layer of doped P3HT polymer chains. Here, a positive quantity represents electron transfer from the inorganic surface to the organic doped P3HT chains (i.e., hole transfer from the organic P3HT chain to the inorganic surface [cyan colour]). In both cases, this charge transfer induces a de-doping effect, leading to a reduction of holes in the p-type P3HT chains. This de-doping effect is more pronounced for doped P3HT on the TeO_2 surface compared to doped P3HT on the Te surface. However, it is essential to note that the charge transfer and de-doping effect are only observed for the first two layers of P3HT chains and diminish for greater distances from the inorganic surface. A more detailed analysis of the mechanism of charge transfer can be found in the Supporting Information. This charge transfer phenomenon plays a crucial role in understanding the thermoelectric trends in these hybrid systems.

We now discuss the Seebeck and conductivity trend as function of Te content. Interestingly, while the Seebeck coefficient increases monotonically, the electrical conductivity of the films exhibits a peak with increasing Te in our hybrid films. Standard binary models in literature are not able to explain these non- monotonic trends of Seebeck and electrical conductivity in our hybrid films [Fig. S13].[33] N. E. Coates later proposed a series-connected model for these hybrid materials that includes a highly conductive layer between the Te nanowires and polymer matrix can accurately describes the Seebeck and electrical conductivity trend in these hybrid materials.[22] We have further shown that high conductive interfacial layer occurs due to strong templating effect at interface using MD simulation. Therefore, total conductivity of TeNW-P3HT hybrid can be written as:

$$\sigma_{eff} = x_{Te}\sigma_{Te} + x_{interface}\sigma_{interface} + x_{P3HT}\sigma_{P3HT} \quad (5)$$

where σ_{eff} is the conductivity of the hybrid material, x_{Te} is the fraction of TeNW, σ_{Te} is the conductivity of the Te nanowires, x_s is the fraction of the interfacial component, σ_s is the conductivity of the interfacial layer, x_{P3HT} is the P3HT matrix fraction, and σ_{P3HT} is the matrix conductivity. Seebeck coefficient can be written as:

$$S = \frac{x_{Te}S_{Te}\sigma_{Te} + x_{interface}S_{interface}\sigma_{interfeace} + x_{P3HT}S_{P3HT}\sigma_{P3HT}}{\sigma_{eff}} \quad (6)$$

At lower TeNW content (<10%), P3HT matrix dominates the transport. Therefore, a similar value of power factor is observed for P3HT-TeNW and P3HT-TeO_2NW hybrid materials. As the nanowire content increases, both the templating effect and charge transfer between NWs and P3HT interface increases. While templating gives rise to a higher mobility at interface, charge transfer at interface introduces de-doping which enhances Seebeck coefficient of interface layer. Both these factor controls the conductivity and Seebeck coefficient trend in P3HT-TeNW and P3HT-TeO_2NW hybrid materials as discussed in Table 1.[22,24]

	Templating effect	De-doping due to Charge transfer at interface	Seebeck and conductivity	Discussion
P3HT	X	X	x	
P3HT-TeNWs (10%-60%)	$\mu(\uparrow)$	$n_{de-doping}(\downarrow)$ $S_{de-doping}(\uparrow)$	$\sigma = n_{de-doping}(\downarrow) \times e \times \mu(\uparrow)$ $S(\uparrow) \propto \frac{1}{n_{de-doping}(\downarrow)}$	Conductivity increases due to Strong templating compared to reduction in carrier concentration; Seebeck coefficient increases due to charge transfer induced de-doping at interface. Strong templating take over carrier concentration reduction to improve the conductivity
P3HT-TeNWs (70%-90%)	$\mu(\uparrow)$	$n_{de-doping}(\downarrow)$ $S_{de-doping}(\uparrow)$	$\sigma = n_{de-doping}(\downarrow) \times e \times \mu(\uparrow)$ $S(\uparrow) \propto \frac{1}{n_{de-doping}(\downarrow)}$	Conductivity stays constant due to comparable *n* reduction rate and templating effect; Seebeck increases due to charge transfer induced de-doping.
P3HT-TeO_2NWs (10%-40%)	$\mu(\uparrow)$	$n_{de-doping}(\downarrow)$ $S_{de-doping}(\uparrow)$	$\sigma = n_{de-doping}(\downarrow) \times e \times \mu(\uparrow)$ $S(\uparrow) \propto \frac{1}{n_{de-doping}(\downarrow)}$	Conductivity increases due to templating compared to reduction in carrier concentration; Seebeck coefficient increases due to charge transfer induced de-doping at interface. Templating take over carrier concentration reduction to improve the conductivity
P3HT-TeO_2NWs (40%-90%)	$\mu(\uparrow)$	$n_{de-doping}(\downarrow)$ $S_{de-doping}(\uparrow)$	$\sigma = n_{de-doping}(\downarrow) \times e \times \mu(\uparrow)$ $S(\uparrow) \propto \frac{1}{n_{de-doping}(\downarrow)}$	Conductivity drops due to stronger *n* reduction rate as observed in charge transfer section in DFT and weak templating effect; Seebeck increases due to charge transfer induced de-doping.

Table 1: Summary of physical phenomena contributing to thermoelectric trends at P3HT-TeNWs and P3HT-TeO_2NWs interface.

Conclusions

In summary we have demonstrated that the TE properties in P3HT-TeNWs hybrid systems can be significantly enhanced by controlling the oxidation of the Te NWs during the synthesis, followed by a strong templating effect. TEM study revealed amorphous oxidation on the Te NW surface for oxidised samples whilst for oxidation-controlled samples, no oxidation was detected. MD simulation demonstrated a strong uni-directional templating effect of P3HT on a Te surface compared to a TeO_2 surface which resulted in a multi-directional templating of P3HT. DFT calculations reveal strong de-doping effects at the TeO_2-P3HT interface compared to a Te-P3HT

interface. To the best of our knowledge, a power factor of 64.8 $\mu W/mK^2$ is the highest value reported for the P3HT-TeNWs hybrid system to date. Our work provides a new direction to improve TE properties, and in general, charge transport in hybrid TE materials.

Acknowledgments

S.S., P.K., and K.H. would like to acknowledge funding from the Accelerated Materials Development for Manufacturing Program at A*STAR via the AME Programmatic Fund by the Agency for Science, Technology, and Research under Grant No. A1898b0043. S. S. and I.N. would like to thank A*STAR Graduate Academy's ARAP programme for funding S.S.'s graduate studies in IMRE, A*STAR. I.N. wishes to acknowledge financial support by the Engineering and Physical Sciences Research Council (EPSRC) for Grant No. EP/T026219/1.

Materials and Methods

Reagents

Ethylene glycol (>99% EG, Sigma Aldrich, anhydrous), polyvinylpyrrolidone (PVP-K30, M.W. ~ 40,000, Fluka), potassium hydroxide (≥ 85% KOH basis, pellets, white, Merck), tellurium dioxide (99.995% TeO_2, Aldrich), hydrazine hydrate (N_2H_4 50-60%, Sigma Aldrich), Poly(3-hexylthiophene-2,5-diyl) (M.W. ~50-70kDa, regioregular electronic grade, Rieke Metals), iron trichloride (≥ 99.99% , anhydrous, powder, Aldrich), acetonitrile (98%, Sigma Aldrich), chloroform (>99%, anhydrous, Sigma Aldrich), were used as supplied without further purification.

Synthesis of Inorganic-Organic Nanocomposites

The inorganic nanostructures of tellurium nanowires (TeNWs) were synthesized via an aqueous solution route following established literature protocols.[34] Poly (3-hexylthiophene) P3HT was dissolved in chloroform to obtain a stock solution (10mg/mL) followed by magnetic stirring at 40℃ on a hotplate for 30 mins. The desired amount of polymer solution was added to various weight percentages (10% to 90%) of tellurium nanowires (TeNWs). These solutions were power sonicated for 60 mins in pulse mode (15 sec ON and 5 sec OFF) to obtain a homogenous dispersion before being drop-casted onto Si and quartz substrates.

Thin Film Fabrication

The solutions were drop casted onto round quartz substrates of 20 mm diameters for thermoelectric (TE) transport properties measurements. For X-ray diffraction (XRD), scanning electron microscopy (SEM), and X-ray photoelectron spectroscopy (XPS) analysis, films were drop casted onto (1×1) cm^2 Si substrates at 70°C on a hotplate. The drop casted films were annealed at 100°C overnight inside a nitrogen filled glovebox to remove any solvent present. For doping the fabricated hybrid films, $FeCl_3$ was dissolved in acetonitrile at various molar concentrations of $FeCl_3$. The hybrid films were immersed into the $FeCl_3$ solution followed by rapid drying to maintain uniformity of the films. The films were not exposed to air at any point. Prior to drop casting, all substrates were cleaned by sequential sonication in acetone and isopropanol for 10 mins each, followed by UV-ozone exposure at 100°C for 10 min.

Characterization

Focused ion beam (FIB) cross-sectioning of the drop-casted nanowires was carried out on a Zeiss Crossbeam 540 equipped with carbon GIS and Ga ion source. Three amorphous carbon layers as first deposited onto the nanowires, including a 20 nm layer via pre-sputtering outside FIB chamber, a 50 nm layer via e-beam, and a 700 nm layer via ion-beam. Ga ion-beam was used for the FIB lamella preparation. The sample was finally fine-polished using a 30kV 50pA probe and cleaned using a 5kV 10pA probe. The X-ray diffraction patterns were collected using a Bruker D8 Advanced X-ray powder diffractometer with Cu Kα radiation at room temperature. X-ray photoelectron spectroscopy (XPS) was performed using an AXIS Supra spectrometer (Kratos Analytical, UK) equipped with a hemispherical analyzer and a monochromatic Al Kα source (1487 eV) operating at 15 mA and 15 kV. The XPS spectra were acquired over an analysis area of 700×300 μm^2 at a take-off angle of 90º. A pass energy of 160 and 20 eV was used for survey and high-resolution scans, respectively. Charge compensation was achieved by using low energy electron flooding. Deconvolution of the raw data was performed using the Casa XPS software. Scanning electron microscopy (SEM) imaging was performed on a JEOL JSM 7800F Prime-scanning electron microscope (SEM) at an operating voltage of 5 keV. To perform Transmission electron microscopy (TEM) analysis, samples were prepared by drop casting a 20 µL solution on a standard 3 mm copper mesh grid with a continuous lacey carbon coated film (Cat. No. 3830C-CF, SPI Supplies, West Chester, USA). Suspension solutions were prepared by mixing 50 µg of powder containing the nanowires (TeNWs or P3HT-TeNWs) into 1 mL ACS-grade water (Cat.

No. 320072, Sigma-Aldrich Co. LLC, St. Louis, USA). The suspension solutions were thoroughly mixed using a vortex mixer (Scientific Industries Inc., New York, USA) for 2 minutes prior to dip casting on the TEM grid to uniformly disperse the nanoparticles in the solution. Grids were naturally dried for about 1 hour prior to loading inside the TEM. Grid samples were loaded onto a standard low-background TEM double tilt holder (Thermo Fisher Scientific, Waltham, MA USA). TEM images were acquired using a Titan 80-300 keV and Tecnai G2 80-200 keV TEMs (Thermo Fisher Scientific, Waltham, MA USA; formerly produced by FEI) equipped with a 4096×4096 pixels^2 OneView CMOS camera (Gatan, Inc., Pleasanton, CA, USA). TEM images were processed using Digital Micrograph (DM) (Gatan, Inc., Pleasanton, CA, USA) and open-source ImageJ (National Institutes of Health) software to enhance the contrast and brightness.

Thermoelectric Measurements

Seebeck coefficient of TE hybrid films were measured with a Portable Thermoelectric Meter (PTM-3, Joule Yacht) with 0.1μV/K resolution of Seebeck coefficient, and temperature gradient (ΔT) of 25°C between hot and cold probe ends (~ 5mm apart). The company claims the measurement error of ±7%. To ensure the consistency of the results, the thermoelectric properties were verified using a cryostat probe station, as depicted in SI Fig. S12. The thicknesses of fabricated films were estimated by Alpha-Step IQ surface profiler. Films were scratched at center with a toothpick and scanned at various points to analyze the uniform thickness of the films. Electrical conductivity measurements were carried out with typical four-point probe set up using Keithley 2450 source meter. After obtaining the IV characteristics curves, sheet resistance was multiplied with geometric factor as reported in the literature,[35] which then were multiplied with thickness of films to obtain resistivity (ρ) values, then electrical conductivity (σ) of films was calculated by using equation $\sigma = 1/\rho$. Finally, the power factor (PF) of TE materials was calculated as $PF = S^2\sigma$. Several samples were used for the measurements, and each sample was tested at least 4 times from different points to ensure the reproducibility of the results.

References:

1. Y. Du, J. Xu, B. Paul, P. Eklund, *Appl. Mater. Today* 2018, **12**, 366.
2. J. F. Li, W. S. Liu, L. D. Zhao, M. Zhou, *NPG Asia Mater.* 2010, **2**, 152.
3. A. Balandin, K. L. Wang, *J. Appl. Phys.* 1998, **84**, 6149.

4. M. He, J. Ge, Z. Lin, X. Feng, X. Wang, H. Lu, Y. Yang, F. Qiu, *Energy Environ. Sci.* 2012, **5**, 8351.
5. Y. Wang, S. M. Zhang, Y. *J.* Deng, *Mater. Chem. A* 2016, **4**, 3554.
6. L . Wang, Y. Liu, Z. Zhang, B. Wang, J. Qiu, D. Hui, S. Wang, *Compos. Part B Engineering* 2017, **122**, 145.
7. H. Ju, J. Kim, *Chem. Eng. J.* 2016, **297**, 66.
8. N. T. Kemp, A. B. Kaiser, C. J. Liu, B. Chapman, O. Mercier, A. M. Carr, H. J. Trodahl, R. G. Buckley, A. C. Partridge, J. Y. Lee, C. Y. Kim. *J. Polym. Sci. Part B Polym. Phys.* 1999, **37**, 953.
9. G. H. Kim, D. H. Hwang, S. I. Woo, *Phys. Chem. Chem. Phys.* 2012, **14**, 3530.
10. C. J. An, Y. C. Lee, Y. H. Kang, S. Y. Cho, *Carbon N. Y.* 2017, **124**, 662.
11. Z. Liang, M. J. Boland, K. Butrouna, D. R. Strachan, K. R. Graham, *J. Mater. Chem. A* 2017, **5**, 15891.
12. H. Ju, J. Kim, *ACS Nano* 2016, **10**, 5730.
13. S. Ma, K. Anderson, L. Guo, A. Yousuf, E. C. Ellingsworth, C.Vajner, H. T. Wang, G. Szulczewski, *Appl. Phys. Lett.* 2014, **105***,* 073905.
14. C. Li, F. Jiang, C. Liu, W. Wang, X. Li, T. Wang, J. Xu, *Chem. Eng. J.* 2017, **320**, 201.
15. X. Hu, K. Zhang, J. Zhang, S. Wang, Y. Qiu, *ACS Appl. Energy Mater.* 2018, **1**, 4883.
16. W. Thongkham, C. Lertsatitthanakorn, K. Jiramitmongkon, K. Tantisantisom, T. Boonkoom, M. Jitpukdee, K. Sinthiptharakoon, A. Klamchuen, M. Liangruksa, P. Khanchaitit, *ACS Appl. Mater. Interfaces* 2019, **11**, 6624.
17. B. Zhang, J. Sun, H. E. Katz, F. Fang, R. L. Opila, *ACS Appl. Mater. Interfaces* 2010*,* **2**, 3170.
18. A. Sahu, B. Russ, N. C. Su, J. D. Forster, P. Zhou, E. S. Cho, P. Ercius, N. E. Coates, R. A. Segalman, J. J. Urban, *J. Mater. Chem. A* 2017, **5**, 3346.
19. M. P. Gordon, K. Haas, E. Zaia, A. K. Menon, L. Yang, A. Bruefach, M. D. Galluzzo, M. C. Scott, R. S. Prasher, A. Sahu, J. J. Urban, *Adv. Electron. Mater.* 2021, **7**, 2000904.
20. L. Wang, Q. Yao, W. Shi, S. Qu, L. Chen, *Mater. Chem. Front.* 2017, **1**, 741.
21. Q. Yao, L. Chen, W. Zhang, S. Liufu, X. Chen, *ACS Nano* 2010, **4**, 2445.
22. N. E. Coates, S. K. Yee, B. McCulloch, K. C. See, A. Majumdar, R. A. Segalman, J. J. Urban, *Adv. Mater.* 2013, **25**, 1629.
23. J. Choi, J. Y. Lee, S. S. Lee, C. R. Park, H. Kim, *Adv. Energy Mater.* 2016, **6***,*1502181.
24. P. Kumar, E. W. Zaia, E. Yildirim, D. M. Repaka, S. W. Yang, J. J. Urban, K.

Hippalgaonkar, *Nat. Commun.* 2018, **9**, 1.

25. D. X. Crispin, *Energy Environ. Sci.* 2012.
26. S. D. Kang, G. J. Snyder, *Nat. Mater.* 2017, **16***,* 252.
27. A. Zavabeti, P. Aukarasereenont, H. Tuohey, N. Syed, A. Jannat, A. Elbourne, K. A. Messalea, B. Y. Zhang, B. J. Murdoch, J. G. Partridge, M. Wurdack, *Nat. Electron.* 2021, **4**, 277.
28. S. Liu, N. Peng, Y. Bai, D. Ma, F. Ma, K. Xu, *RSC Adv.* 2016, **6**, 31668.
29. M. K. Han, S. Kim, H. Y. Kim, S. J. Kim, *RSC Adv.* 2013, **3**, 4673.
30. J. Sahadevan, S. E. Muthu, P. Sivaprakash, I. Kim, N. Padmanathan, E. Eswaramoorthi, 2023,1.
31. G. J. Snyder, E. S. Toberer, *Nat. Mater.* 2008, **7**, 105.
32. G. Chen, A. Shakouri, *J. Heat Transfer* 2002, **124**, 242.
33. Y. Gelbstein, *J. Appl. Phys.* 2009, **105**, 023713.
34. G. Zhang, B. Kirk, L. A. Jauregui, H. Yang, X. Xu, Y. P. Chen, Y. Wu, *Nano Lett.* 2012, **12**, 56.
35. F. M. Smits, *Bell Syst. Tech. J.* 1958, **37**, 711.
36**.** S.R. Bhopale, M.A. More, *Physica status solidi (A)*. 2022, **219**, 2200126.
37. N.G. Semaltianos, S. Logothetidis, N. Hastas, W. Perrie, S. Romani, R.J. Potter, G. Dearden, K.G. Watkins, P. French, M. Sharp, *Chem. Phys. Lett.* 2010, **484**, 283-9.
38. D. Bash, Y. Cai, V. Chellappan, S.L. Wong, X. Yang, P. Kumar, J.D. Tan, A. Abutaha, J.J. Cheng, Y.F. Lim, S.I. Tian, *Adv. Func. Mater.* 2021, **31**, 2102606.